Konya Mühendislik Bilimleri Dergisi, c.14, s.3, 1105-1124, 2026
Konya Journal of Engineering Sciences, v.14, n.3, 1105-1124, 2026
ISSN: 2667-8055 (Electronic)
DOI: 10.36306/konjes.1826817

SURFACE ROUGHNESS INFLUENCE ON THE HYDRAULIC PERFORMANCE OF AN API 610 BB3 MULTISTAGE CENTRIFUGAL PUMP: AN EXPERIMENTAL–CFD STUDY

[1,*]Sinan GÜNGÖR, [2]Abdulkerim OKBAZ, [3]Zehra YUMURTACI

[1]*Standart Pompa ve Makina San. Tic. A.Ş, DOSB Umraniye, Istanbul 34775, Turkey*
[2,3]*Faculty of Mechanical Engineering, Yildiz Technical University, Istanbul 34349, Turkey*
[1]sinan@standartpompa.com , [2]aokbaz@yildiz.edu.tr, [3]zyumur@yildiz.edu.tr

Highlights

- Experimental and CFD study on an API 610 BB3 multistage pump
- Effect of surface roughness ks = 0–25–50–73 μm on head and efficiency
- Head and efficiency reductions are linked to casting-induced surface defects

***Corresponding Author:** Sinan GÜNGÖR, sinan@standartpompa.com

Konya Mühendislik Bilimleri Dergisi, c.14, s.3, 1105-1124, 2026
Konya Journal of Engineering Sciences, v.14, n.3, 1105-1124, 2026
ISSN: 2667-8055 (Electronic)
DOI: 10.36306/konjes.1826817

SURFACE ROUGHNESS INFLUENCE ON THE HYDRAULIC PERFORMANCE OF AN API 610 BB3 MULTISTAGE CENTRIFUGAL PUMP: AN EXPERIMENTAL–CFD STUDY

[1,*]Sinan GÜNGÖR, [2]Abdulkerim OKBAZ, [3]Zehra YUMURTACI

[1]*Standart Pompa ve Makina San. Tic. A.Ş, DOSB Umraniye, Istanbul 34775, Turkey*
[2,3]*Faculty of Mechanical Engineering, Yildiz Technical University, Istanbul 34349, Turkey*
[1]sinan@standartpompa.com, [2]aokbaz@yildiz.edu.tr, [3]zyumur@yildiz.edu.tr

(Received: 19.11.2025; Accepted in Revised Form: 30.12.2025)

ABSTRACT: Surface roughness affects the hydraulic performance and energy efficiency of API 610 BB3 (between-bearings, axially split, multistage) pumps used in oil, gas, and petrochemical service. We quantify its impact using experiments and computational fluid dynamics (CFD). A four-stage pump was tested at 2900 rpm on a closed-loop rig, and head–flow-rate (Q–H_m) and efficiency–flow-rate (Q–η) characteristics were measured over 30–90 m³/h. Surface roughness of the main hydraulic components was measured using a profilometer and represented in the numerical model by equivalent sand-grain roughness values k_s = 0, 25, 50, and 73 μm applied to all wetted walls. Three-dimensional Reynolds-averaged Navier–Stokes (RANS) simulations were performed using the SST k–ω turbulence model with rough-wall functions on a domain including leakage and return channels. The k_s = 73 μm case agrees with the measured curves, with the efficiency deviation limited to ~4.1% within 45–90 m³/h, whereas larger deviations occur at 30 m³/h due to part-load operation. Near the best-efficiency region, increasing k_s from 0 to 73 μm reduces head by 5.94% and efficiency by 6.62 percentage points. Neglecting roughness overestimates performance; realistic roughness is required for CFD-based prediction of API 610 BB3 pumps.

Keywords: *API 610 BB3, Centrifugal Pump, CFD, Hydraulic Performance, Multistage Pump, Surface Roughness*

NOMENCLATURE

k_s	equivalent sand-grain roughness (μm)
Q	volumetric flow rate (m³/h)
H_m	head (m)
P_e	electrical input power (kW)
P_h	hydraulic power (kW)
P_s	shaft power (kW)
η_h	hydraulic efficiency (%)
η	pump efficiency (%)
η_m	mechanical efficiency (%)

ABBREVIATIONS

API	American Petroleum Institute
BB3	Between-bearings, axially split multistage pump
CFD	Computational Fluid Dynamics
RANS	Reynolds-Averaged Navier-Stokes
SST k-ω	Shear Stress Transport turbulence model
MRF	Multiple Reference Frame
SIMPLE	Semi Implicit Method for Pressure Linked Eq.

***Corresponding Author:** Sinan GÜNGÖR, sinan@standartpompa.com

1. INTRODUCTION

Pumps, which are indispensable machines in industrial applications, convey liquids to a certain head by transferring the rotational energy supplied by the impeller to the fluid [1]. In such impeller pumps, the energy transferred from the rotating impeller increases the pressure and kinetic energy of the liquid, thereby generating the required head within the flow passages between the impeller and the casing [2]. In industrial processes, power plants, and petrochemical applications that demand high heads and high reliability, multistage horizontal BB3 (between-bearings, axially split, multistage centrifugal) pumps designed in accordance with the API 610 standard are widely used as critical equipment [3]. The performance of such pumps can vary significantly depending not only on the design parameters but also on manufacturing quality, surface roughness, and operating conditions. In particular, surface roughness increases hydraulic losses, leading to reductions in head and efficiency and, consequently, to higher energy consumption. Numerical casting simulations carried out by Mohammadian et al. [4] on a BB3-6×6 casing have shown that design decisions such as mold (gating) and feeder layout strongly influence shrinkage defects and surface quality, and therefore, the final hydraulic performance is already shaped at the production stage.

With advances in computational fluid dynamics (CFD), it has become possible to investigate internal flows in pumps in detail and to analyze the effects of design parameters and surface conditions on hydraulic performance. CFD has been applied to multistage centrifugal pumps with realistic industrial geometries, enabling the evaluation of complex internal flow structures and performance trends [5], [6]. Existing studies addressing surface roughness effects in centrifugal pumps can be broadly divided into three groups. The first group focuses on surface modification strategies, including polymeric coatings and composite impellers with reduced surface roughness, aimed at improving hydraulic performance and energy efficiency. Ulaganathan and Karuppuswamy [7] investigated the influence of internal surface coatings on the performance of a single-stage centrifugal pump and showed, through combined experiments and SST k–ω-based CFD simulations, that epoxy and polyurethane coatings reduce the arithmetic mean roughness of hydraulic surfaces, resulting in increased efficiency and reduced input power, while causing only minor changes in head and flow rate at the duty point. Similarly, Kocaaslan et al. [8] demonstrated that reducing the surface roughness of the impeller and volute of a single-stage centrifugal pump by applying a polyurethane coating leads to increases in head and efficiency. Deshmukh et al. [9] examined the effect of casing surface roughness and ceramic-filled epoxy coatings on centrifugal pump performance and reported that increasing casing roughness from 100 to 300 μm causes head reductions of approximately 9–15%, whereas coating the casing with an ultra-smooth ceramic-filled epoxy improves efficiency by up to about 9.6% with only minor changes in input power. Papageorgiou et al. [10] showed that replacing a cast-iron impeller with a 3D-printed composite impeller of lower surface roughness increases pump efficiency by approximately 15%, as confirmed by both experimental measurements and numerical simulations.

The second group of studies introduces equivalent sand-grain roughness into RANS-based CFD frameworks to quantify roughness effects more explicitly. Lipej et al. [11] analyzed the influence of internal wall roughness on the efficiency of a single-stage centrifugal pump (n_q = 24 min^{-1}) by modelling different equivalent sand-grain roughness heights in CFD and comparing the results with experiments. Their results showed that roughness has a limited effect under part-load conditions but can cause efficiency losses exceeding 10 percentage points at high flow rates, and that a measured roughness of $R_a \approx 5$ μm can be reasonably represented by an equivalent sand-grain roughness of approximately 50 μm. He et al. [12] examined the effect of internal wall roughness on the hydraulic performance of a double-channel sewage pump by combining experiments with CFD using the standard k–ε turbulence model and equivalent

sand-grain roughness. In their study, the measured arithmetic mean roughness R_a was converted into an equivalent sand-grain roughness height k_s using the correlation $k_s = 5.863R_a$, and these k_s values were prescribed in the wall functions of the CFD model. Increasing k_s resulted in a marked rise in shaft power and noticeable reductions in head and efficiency. Lim and Sohn [13] showed that internal surface roughness reduces centrifugal pump efficiency by approximately 3.0% by solving the RANS equations with the standard $k–\varepsilon$ turbulence model and roughness-modified wall functions; R_a values of 100 μm were applied to the impeller and volute casing and 30 μm to the inlet and outlet casings using the correlation $k_s = 1 - 1.3R_a$. Liang et al. [14] numerically investigated the influence of wall roughness on pressure distribution and hydraulic performance in a large three-blade centrifugal dredge pump using the SST $k–\omega$ turbulence model and an equivalent sand-grain wall function based on $k_s = 5.863\ R_a$. Their results indicated three roughness regimes: hydraulically smooth ($k_s < 8$ μm), transitional ($8 < k_s < 50$ μm), and fully rough ($k_s > 50$ μm). For k_s values exceeding 50 μm, pump efficiency decreased sharply while shaft power increased almost linearly. Chang et al. [15] applied an equivalent sand-grain roughness model to a self-priming centrifugal pump and showed that increasing wall roughness leads to reductions in head and efficiency, while quantifying roughness-induced energy losses using entropy generation analysis.

The third group includes advanced modelling approaches and direct comparisons between smooth-wall CFD predictions and measurements obtained on pumps with realistic rough surfaces. Torner, Duong, and Wurm [16] proposed the Discrete Porosity Method to represent rough surface effects without resolving the full surface topology by introducing a drag-related sink term in the momentum equations derived from the Darcy–Forchheimer formulation. The method was first applied to channel-flow simulations to determine an equivalent sand-grain roughness of $k_s = 175$ μm for cast iron and was subsequently implemented in a turbopump CFD model, reproducing experimental head and efficiency characteristics within a few percent. Benigni et al. [17] carried out a combined numerical and experimental investigation on a low specific speed, API-compliant, double-volute single-stage centrifugal pump and showed that smooth-wall CFD assumptions systematically overpredict head compared with measurements obtained on pumps with realistic cast surfaces. Juckelandt et al. [18] investigated the performance and loss mechanisms of low specific speed centrifugal pumps ($n_q = 13.4$ min^{-1}) by comparing hydraulically smooth surfaces ($R_a \leq 0.4$ μm) with realistic rough surfaces implemented using laser-structured foils corresponding to an equivalent sand-grain roughness of $k_s = 60$ μm. Their results showed that surface roughness reduces the hydraulic efficiency by 5.3%, corresponding to a decrease of 3.8 percentage points, at the best efficiency point. At part-load operation, the efficiency reduction increased to 6.9%, whereas at overload conditions the reduction was 4.2%.

Although existing studies demonstrate that internal surface roughness can alter pump performance, most investigations are limited to single-stage configurations, simplified geometries, or purely numerical representations of roughness. To date, no systematic study has examined a multistage API 610 BB3 pump with realistic cast surfaces, in which roughness simultaneously affects both impeller and casing components, using a combined experimental and CFD-based approach. In this context, the present work focuses on a BB3-type multistage centrifugal pump and quantifies the effects of different equivalent sand-grain roughness levels (k_s = 0, 25, 50, and 73 μm) on the head–flow-rate and efficiency–flow-rate characteristics at 2900 rpm, based on joint experimental measurements and validated SST $k–\omega$ simulations. By directly relating measured surface roughness to hydraulic performance, we address three aspects: (i) the combined influence of surface roughness on the characteristic curves of a multistage BB3 pump, (ii) the efficiency penalties associated with different roughness levels over the operating range, and (iii) implications for roughness-modelling strategies in CFD analyses of API 610 BB3 pumps.

2. MATERIAL AND METHODS

2.1. Experimental Setup

2.1.1 Test Pump and Facility

Experimental studies were conducted on a horizontal, four-stage, axially split, between-bearings (BB3-type) centrifugal pump. The pump was manufactured by Standart Pompa ve Makine San. A.Ş. and designed in full compliance with the API 610 standard for BB3 pumps. Such pumps are widely used in oil refineries, petrochemical plants, and high-pressure fluid transfer systems. The internal structure of the test pump is shown in Figure 1. It has four radial impellers mounted on a common shaft and arranged in series within a central drum. The volute casing is horizontally split into upper and lower halves *to* facilitate assembly and inspection. Each impeller is equipped with wear rings at both the inlet and outlet to limit internal leakage and preserve hydraulic performance. Mechanical seals are used to prevent leakage along the shaft. Bearing housings support the rotor and accommodate both radial and axial loads.

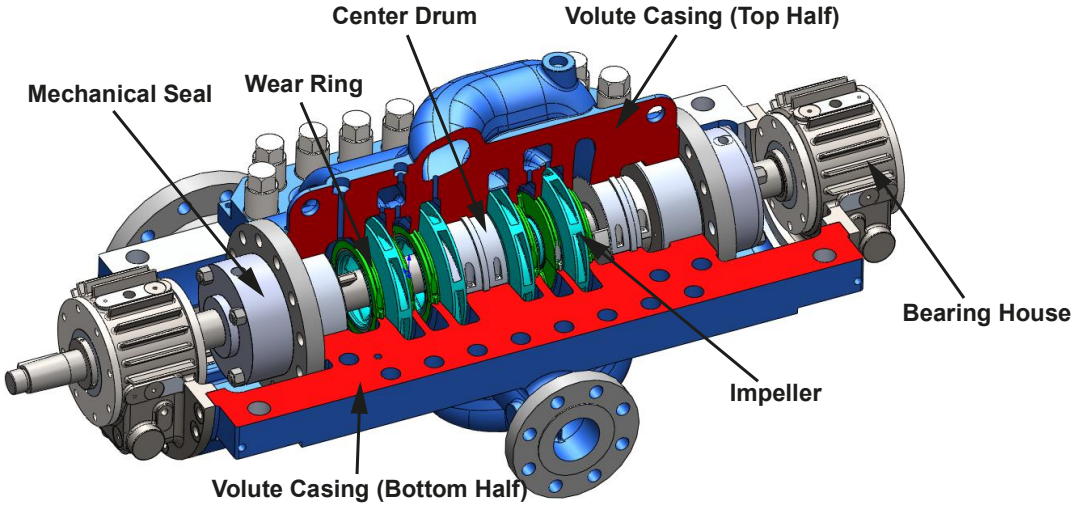

Figure 1 Internal structure of the API 610 BB3 test pump

The experiments were carried out in the Standart Pompa ve Makina San. A.Ş. test laboratory. The test facility enables controlled performance measurements of multistage centrifugal pumps under variable discharge conditions. The closed-loop circuit consists of a water tank, suction and discharge pipelines, and an electromagnetic flowmeter for flow-rate measurement. Pressure transmitters are installed at the pump inlet and outlet to record suction and delivery pressures. The setup also includes a motor–pump coupling system, a variable-frequency drive for speed control, and a throttling valve located on the discharge line. Hydraulic performance tests were conducted in accordance with the BS EN ISO 9906:2012 standard for rotodynamic pumps [19].

The pump was mounted in a suction-lift configuration, as shown in Figure 2. The suction line was connected to the supply tank, and the discharge flow returned to the same tank. Clean water at ambient temperature served as the working fluid. Since the pump was designed for a working fluid with ρ = 850 kg/m^3 and the motor was selected accordingly, the motor power limit was reached at Q = 90 m^3/h during the water-based performance test; therefore, the experimental data are reported up to 90 m^3/h. The suction and discharge pipe diameters were DN80 and DN65, respectively. Because of the difference in cross-sectional areas, the velocity head correction was included in the total head calculation.

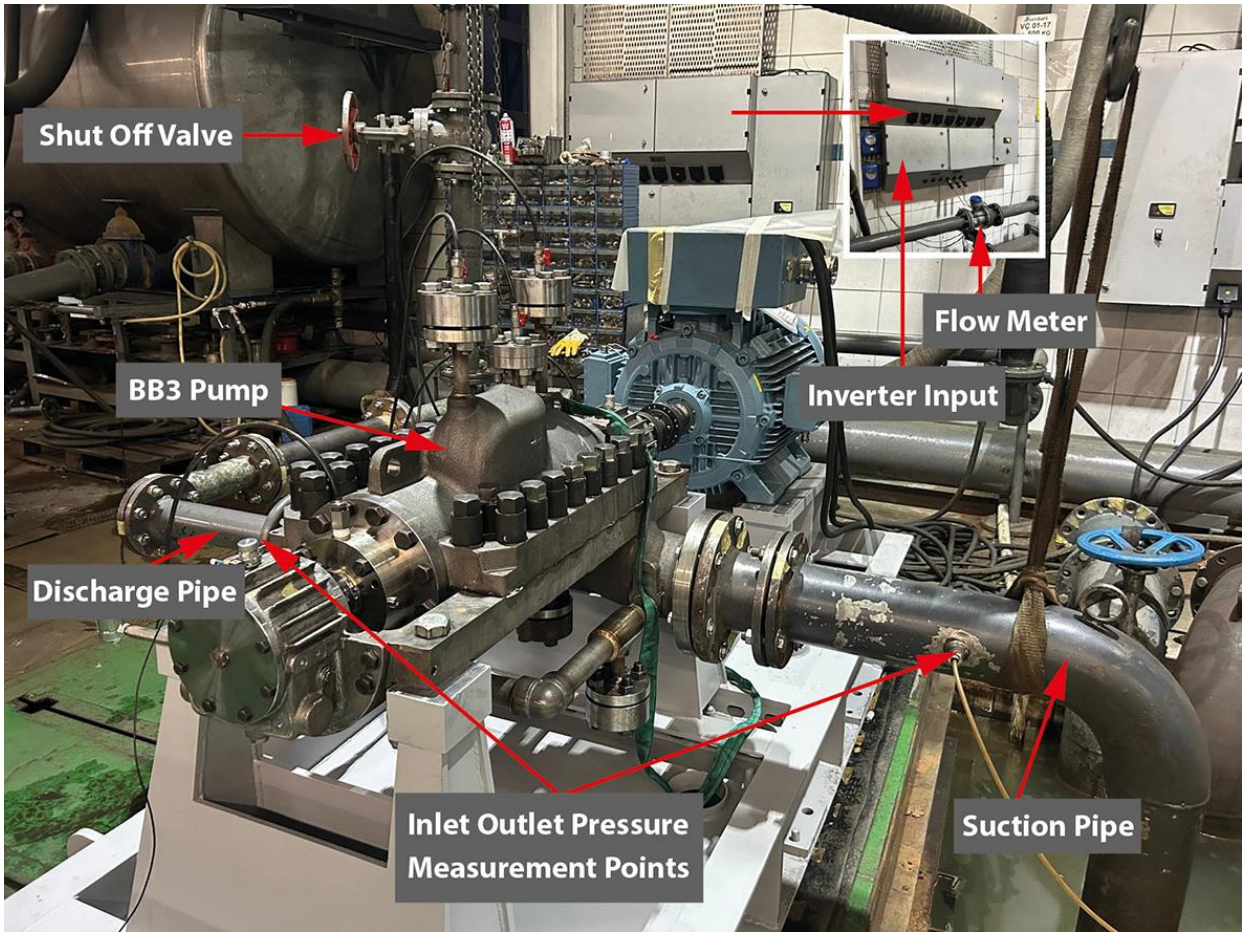

Figure 2. Experimental pump test rig

Before testing, surface roughness measurements were taken on the main hydraulic components using a stylus-type profilometer (Figure 3). Measurements were performed on the pressure and suction sides of the impeller blades and on selected regions of the volute wall. The arithmetic mean roughness was measured as R_a = 12.5 μm

Figure 3. Surface roughness measurement using a contact stylus profilometer

2.1.2 Measurement Instruments and Data Acquisition

The discharge flow rate was measured by a Krohne Optiflux 2000 IFC 050 DN80 electromagnetic flowmeter. The suction pressure was measured with a Keller PR33X absolute pressure transmitter (3 bar), and the discharge pressure with a Keller PR33X G gauge pressure transmitter (30 bar). The motor input power was recorded by a Klemsan Remo-EA power analyzer with 132 kW capacity. All sensors were calibrated prior to testing, and the measurement uncertainty was within ±0.5 % for flow and ±0.25 % for pressure.

At each operating condition, the pump was run until steady values of pressure, flow rate, and power were obtained. Measurements were repeated three times to ensure repeatability. Data acquisition was carried out using a digital logging system.

2.1.3 Head and Performance Calculations

The total head was calculated from the measured suction and discharge pressures, flow velocities, and elevation difference between the measurement points. The calculation followed the steady-flow energy equation in SI base units:

$$H_m = \frac{p_2 - p_1}{\rho g} + \frac{v_2^2 - v_1^2}{2g} + \Delta z \quad (1)$$

Where p_1 and p_2 are the suction and discharge pressures (Pa), ρ is the water density (kg/m^3), g is the gravitational acceleration 9.81 (m / s^2), v_1 and v_2 are the average velocities in the suction and discharge pipes (m / s), and Δz is the elevation difference between the pressure tap locations.

The volumetric flow rate Q was obtained directly from the electromagnetic flowmeter readings. The hydraulic power was calculated as

$$P_h = \rho g Q H_m \quad (2)$$

The electrical input power P_e was measured by the power analyzer, and the pump shaft power P_s was obtained by multiplying P_e by the nominal motor efficiency η_{mot}. In the experiments, the overall pump efficiency η was then calculated using

$$\eta = \frac{P_h}{P_s} \times 100 \quad (3)$$

All measurements were conducted under steady-state conditions, and each operating point was repeated three times to ensure data consistency. The averaged values of total head, flow rate, and power were used to construct the characteristic performance curves for comparison with the numerical results.

The CFD solution provides the hydraulic efficiency η_h of the hydraulic components, whereas the mechanical efficiency η_m was evaluated using the empirical correlations for mechanical losses (bearing, seal and disc friction) proposed by Gülich [20]. The overall pump efficiency was thus obtained as

$$\eta = \eta_h \times \eta_m \quad (4)$$

All efficiency curves presented in this study represent the overall pump efficiency η rather than the purely hydraulic efficiency.

2.2. Numerical Model

2.2.1 Computational Domain and Mesh Generation

The complete 3D fluid domain of the four-stage, axially-split (API 610 BB3) centrifugal pump was extracted from the SolidWorks CAD model. The domain is comprehensive, including the suction and discharge nozzles, all four impeller stages, corresponding volute casings, interstage crossover channels, and the secondary flow paths such as wear ring leakages. The computational mesh was generated in ANSYS Fluent Meshing using fully polyhedral elements. The polyhedral topology was selected because it provides low skewness, requires fewer elements than a tetrahedral mesh of equivalent resolution, and supports stable convergence behavior.

A grid independence study was conducted using three distinct mesh densities (Table 1). The analysis showed that the difference in predicted head (H_m) and efficiency (η) between the 34.8 million-cell grid (Grid 2) and the 48.7 million-cell grid (Grid 1) was less than 0.5%. Consequently, Grid 1, with approximately 48.7 million cells and a minimum orthogonal quality of 0.12, was chosen for all subsequent simulations, ensuring the results were independent of the mesh resolution while balancing computational cost.

Table 1. Mesh independence assessment. Head and efficiency were evaluated at the same operating point for all three grids.

Grid	Number of cells (× 10^6)	H_m (m)	η (%)	Deviation from Grid 1	
				ΔH_m (%)	$\Delta\eta$ (%)
Grid 3	21.92	211.40	69.57	+0.19	−0.33
Grid 2	34.80	211.83	70.13	+0.39	+0.47
Grid 1 (selected)	**48.69**	**211.00**	**69.80**	reference	reference

The overall computational domain, the rotating and stationary zones, and the applied boundary conditions are summarised in Figure 4.

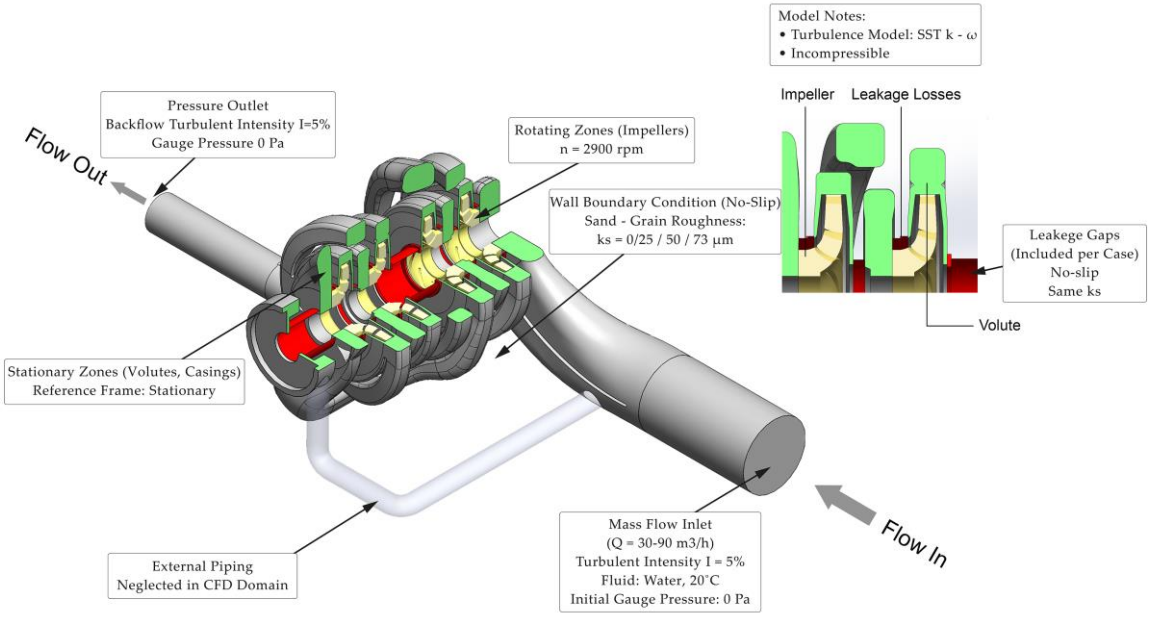

Figure 4. CFD computational domain, boundary conditions and modelling assumptions

2.2.2 Governing Equations

The flow field was modeled as steady, incompressible, and single-phase. The governing equations are based on the Reynolds-Averaged Navier–Stokes (RANS) formulation, which represents the conservation of mass and momentum for the mean flow.

The continuity equation for an incompressible flow is expressed as:

$$\frac{\partial u_i}{\partial x_i} = 0 \tag{5}$$

The momentum equations are expressed in tensor notation as:

$$\rho u_j \frac{\partial (u_i)}{\partial x_j} = -\frac{\partial p}{\partial x_i} + \frac{\partial}{\partial x_j}\left[\mu\left(\frac{\partial u_i}{\partial x_j} + \frac{\partial u_j}{\partial x_i}\right) - \overline{\rho u_i' u_j'}\right] + S_{M,i} \tag{6}$$

Here, u_i and u_j are the mean velocity components, p is the mean pressure, ρ and μ are the constant density and dynamic viscosity, respectively. The last term $S_{M,i}$ represents additional momentum source terms introduced by the Multiple Reference Frame (MRF) formulation, accounting for Coriolis and centrifugal effects in the rotating zones. The term $-\rho\overline{u_i' u_j'}$ corresponds to the Reynolds stresses, which represent the effect of turbulent velocity fluctuations on the mean flow and require a turbulence model for closure.

The Reynolds stresses are related to the mean velocity gradients through the Boussinesq eddy-viscosity hypothesis:

$$\overline{-\rho u_i' u_j'} = \mu_t\left(\frac{\partial u_i}{\partial x_j} + \frac{\partial u_j}{\partial x_i}\right) - \frac{2}{3}\rho k \delta_{ij} \tag{7}$$

Where μ_t is the turbulent (eddy) viscosity, k is turbulence kinetic energy, and δ_{ij} is the Kronecker delta. This assumption allows the Reynolds stresses to be expressed as a function of the mean velocity field and

the turbulent viscosity, thereby converting the RANS equations into a solvable form once a turbulence model is specified.

The turbulent viscosity μ_t was obtained from Menter's Shear Stress Transport (SST) k-ω model. This two-equation eddy-viscosity model combines the accuracy of the standard k–ω formulation in the near-wall region with the robustness of the k-ε formulation in the free-stream region through blending functions F_1 and F_2. The SST model is widely applied in turbomachinery flow simulations due to its ability to accurately predict strong adverse pressure gradients and flow separation phenomena. Recent RANS studies on transonic airfoils have likewise shown that the k–ω SST model provides robust and relatively mesh-insensitive performance among competing turbulence closures, particularly when appropriate near-wall resolution is ensured [21].

The eddy viscosity is computed as:

$$\mu_t = \frac{\rho \alpha_1 k}{\max(\alpha_1 \omega, SF_2)} \tag{8}$$

where $\alpha_1 = 0.31$ is a model constant, S is the magnitude of the mean strain rate, and F_2 is the second blending function ensuring a smooth transition between the near-wall and outer regions.

The SST model introduces two additional transport equations for the turbulence kinetic energy (k) and the specific dissipation rate (ω) under steady-state incompressible flow conditions:

$$\rho u_i \frac{\partial k}{\partial x_i} = \frac{\partial}{\partial x_j}\left[\left(\mu + \frac{\mu_t}{\sigma_k}\right)\frac{\partial k}{\partial x_j}\right] + G_k - Y_k \tag{9}$$

$$\rho u_i \frac{\partial \omega}{\partial x_i} = \frac{\partial}{\partial x_j}\left[\left(\mu + \frac{\mu_t}{\sigma_\omega}\right)\frac{\partial \omega}{\partial x_j}\right] + G_\omega - Y_\omega + D_\omega + S_\omega \tag{10}$$

where G_k and G_ω represent the production of turbulence kinetic energy and the specific dissipation rate, Y_k and Y_ω are the corresponding dissipation terms, and D_ω is the cross-diffusion term. S_k and S_ω are optional user-defined source terms, which are zero for the present simulations. The model constants are $\sigma_k = 0.85$, $\sigma_w = 0.5$.

2.2.3 Rotating Reference Frame Formulation

The interaction between rotating impellers and stationary components was modeled under steady conditions using the Multiple Reference Frame (MRF) method. The additional acceleration terms, $S_{M,i}$ introduced in Eq. (6) were expressed in tensor form as Eq. (11):

$$S_{M,i} = -2\rho\varepsilon_{ijk}\Omega_j u_k - \rho\varepsilon_{ijk}\varepsilon_{klm}\Omega_j\Omega_l r_m \tag{11}$$

where ε_{ijk} is the permutation tensor, Ω_j is the angular velocity vector, and r_m is the position vector relative to the rotation axis. The first term on the right side represents the Coriolis acceleration and the second corresponds to the centrifugal acceleration. The impeller regions were assigned a rotational speed of 2900 rpm. The casings, volutes, and other regions remained stationary. The frozen-rotor approach was used to couple the interfaces between rotating and stationary zones, ensuring mass and momentum conservation.

2.2.4 Surface Roughness Modeling

The SST k-ω model employs a wall function approach to bridge the near-wall region. The core of this study's methodology lies in modifying the wall function to account for surface roughness. Fluent's

standard wall function modifies the logarithmic law of the wall based on the equivalent sand-grain roughness (k_s), a well-established hydraulic parameter in pump analysis. The standard log-law for smooth walls is given by:

$$u^+ = \frac{1}{\kappa} ln(y^+) + B \tag{12}$$

where $u^+ = \frac{u}{u_\kappa}$ and $y^+ = \frac{\rho u_\tau y}{\mu}$

Here $u_\tau = \sqrt{\tau_w/\rho}$ is the friction velocity, $\kappa = 0.41$ is the von Kármán constant, and $B = 5.0$ is the smooth-wall intercept.

For rough walls, the logarithmic velocity profile is shifted downward by a roughness function $\Delta B(k_s^+)$ representing the additional momentum loss induced by the roughness elements:

$$u^+ = \frac{1}{\kappa} \ln(y^+) + B - \Delta B(k_s^+) \tag{13}$$

The nondimensional roughness height is defined as:

$$k_s^+ = \frac{\rho u_\tau k_s}{\mu} \tag{14}$$

As k_s^+ increases, the roughness function $\Delta B(k_s^+)$ becomes larger, leading to an increased wall shear stress (τ_w) and additional head losses. This modification produces a downward shift of the logarithmic velocity profile.

The surface roughness of the pump components was characterized by using the arithmetic average roughness, R_a = 12.5 μm, obtained from profilometric measurements. Since R_a is a geometric descriptor that does not represent the hydraulic resistance encountered by the fluid, it was converted to an equivalent sand-grain roughness height (k_s), which quantifies the same frictional effect as a uniform sand surface. Empirical correlations for machined metallic surfaces in turbulent internal flows typically suggest a ratio of $3 \le k_s / R_a \le 6$ [22]. In this study, a ratio of $k_s / R_a = 5.84$ was adopted, corresponding to k_s = 73 μm. This value is consistent with the expected range for fine-machined steel surfaces and represents the hydraulic equivalent of the measured texture. The adopted k_s = 73 μm value was used as the baseline condition for the numerical analysis. To assess the effect of surface finish on hydraulic losses, additional simulations were performed for k_s = 0, 25, 50, and 73 μm. These cases represent the transition from hydraulically smooth to as-manufactured surfaces. The roughness correction was applied within the wall function, which modifies the local wall shear stress τ_w and near-wall velocity gradient, thus altering the overall energy dissipation and total head predicted by the CFD model. This approach enables accurate representation of the influence of surface roughness on the pump's hydraulic performance without resolving the fine-scale surface geometry.

2.2.5 Solver Configuration and Boundary Conditions

The steady incompressible flow in the four-stage axially split (API 610 BB3) centrifugal pump was solved using the pressure-based finite-volume solver implemented in ANSYS Fluent 2024 R1 on a fully polyhedral mesh. The governing equations for mass, momentum, and turbulence were integrated over each control volume, and surface fluxes were computed to satisfy the conservation laws in discrete form. Pressure–velocity coupling was performed using the SIMPLE algorithm within a segregated solution framework, and the Rhie–Chow momentum interpolation was applied to prevent pressure–velocity decoupling on the collocated grid arrangement.

All convective terms in the momentum and SST k-ω transport equations were discretized using the

Second Order Upwind scheme to provide second-order spatial accuracy and to minimize numerical diffusion in regions with strong streamline curvature and pressure gradients within the impeller and volute passages. Diffusive fluxes were evaluated using central differencing, and gradients were reconstructed by the Least Squares Cell-Based method, which ensures accuracy and stability on unstructured polyhedral meshes. The Warped-Face Gradient Correction was activated to reduce truncation errors resulting from face nonplanarity in curved blade and volute regions. In addition, the High-Order Term Relaxation option was used to stabilize the linearized algebraic system by applying implicit damping to high-order contributions without compromising spatial accuracy. Convergence was considered achieved when scaled residuals of all equations dropped below 10^{-4}, the global mass imbalance was less than 0.01 %, and the monitored total head, shaft torque, and hydraulic efficiency remained constant.

3. RESULTS AND DISCUSSION

3.1. Surface Roughness Effect

Increasing surface roughness adversely affects pump performance along the entire characteristic curve. The Q–H and Q–η curves presented in Figure 5 show that, over the whole flow-rate range, the head and efficiency decrease as the roughness increases.

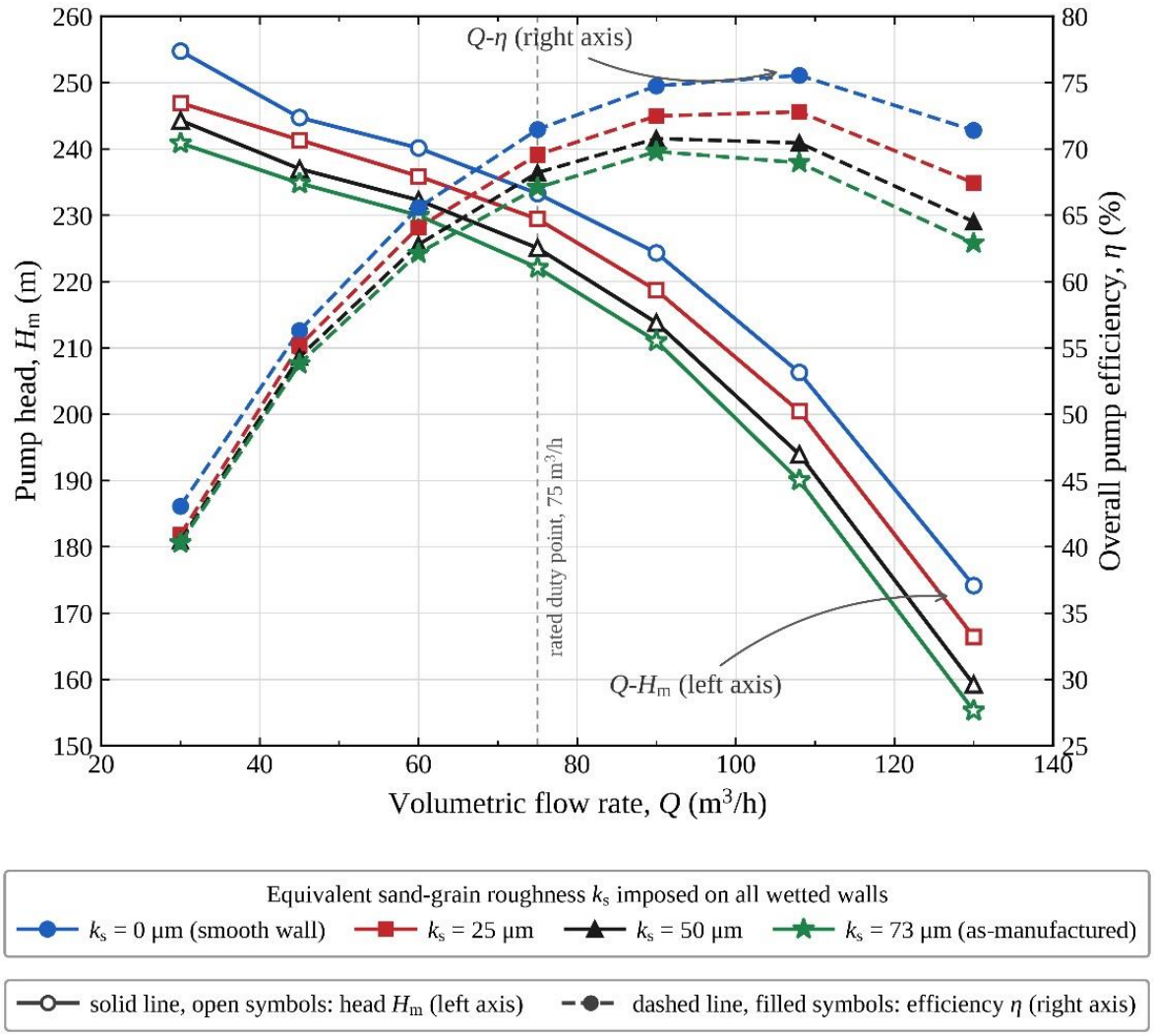

Figure 5. *Q-Hm* and *Q-η* curves for different surface roughness

For the flow rates at which the head differences are most pronounced (90, 75, and 60 m³/h), Table 2 presents the effect of a wall roughness of k_s = 73 μm, relative to the reference case, on pump head and efficiency. The percentage values in the table represent the relative difference between the solutions obtained with different roughness levels; since Q = 75 m³/h corresponds to the pump's rated operating (duty) point, the values at this flow rate are used as an illustrative example. For instance, a ΔH_m of 4.78% at 75 m³/h indicates that the pump head calculated for the smooth-wall case (0 μm) is 4.78% higher than that for the 73 μm roughness case, meaning that reducing the 0 μm result by this percentage yields the corresponding 73 μm value. At high flow rates, the losses in head and efficiency are pronounced, whereas at lower flow rates the variation remains more limited. This finding indicates that the influence of increasing roughness on pump performance does not vary linearly across the operating range.

Table 2. Relative reduction in head and overall efficiency caused by surface roughness, expressed with respect to the as-manufactured case k_s = 73 μm.

Compared roughness levels	Q = 60 m³/h		Q = 75 m³/h (duty point)		Q = 90 m³/h	
	ΔH_m (%)	$\Delta\eta$ (%)	ΔH_m (%)	$\Delta\eta$ (%)	ΔH_m (%)	$\Delta\eta$ (%)
k_s = 0 vs. 73 μm	4.23	5.25	4.78	6.15	5.94	6.62
k_s = 25 vs. 73 μm	2.51	3.02	3.19	3.57	3.51	3.70
k_s = 50 vs. 73 μm	1.00	1.04	1.31	1.67	1.30	1.39

As surface roughness increases, the effective friction and flow resistance rise, and consequently the wall shear stress increases. With increasing flow rate, the rise in relative velocities further intensifies this effect. Figure 6 shows the wall shear stress distribution for 90 m³/h using the same colour scale. A distinct increase in the wall shear stress regions on the impeller and volute walls is observed. This increase is consistent with the corresponding difference in head.

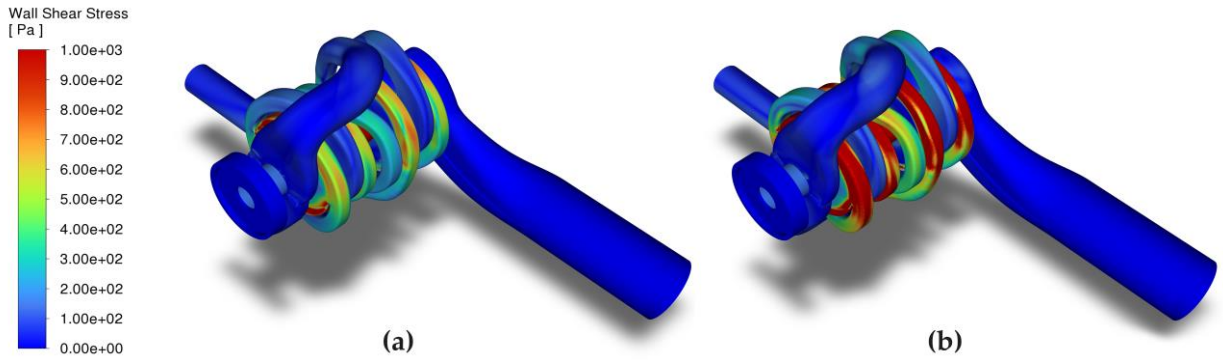

Figure 6. Wall shear stress distribution on the volute for a) smooth wall k_s = 0 μm b) rough wall k_s = 73 μm

The turbulence kinetic energy k contours given in Figure 7 show that, as roughness increases, regions of high turbulence kinetic energy expand, particularly in the impeller outlet region and the tongue–volute interaction zone. Together with the increase in wall shear stress caused by higher roughness, the growth of these high-k regions enhances hydraulic losses. The reduction observed in the Q–H_m and Q–η curves can therefore be explained by the combined increase in losses associated with wall shear stress and turbulence distribution.

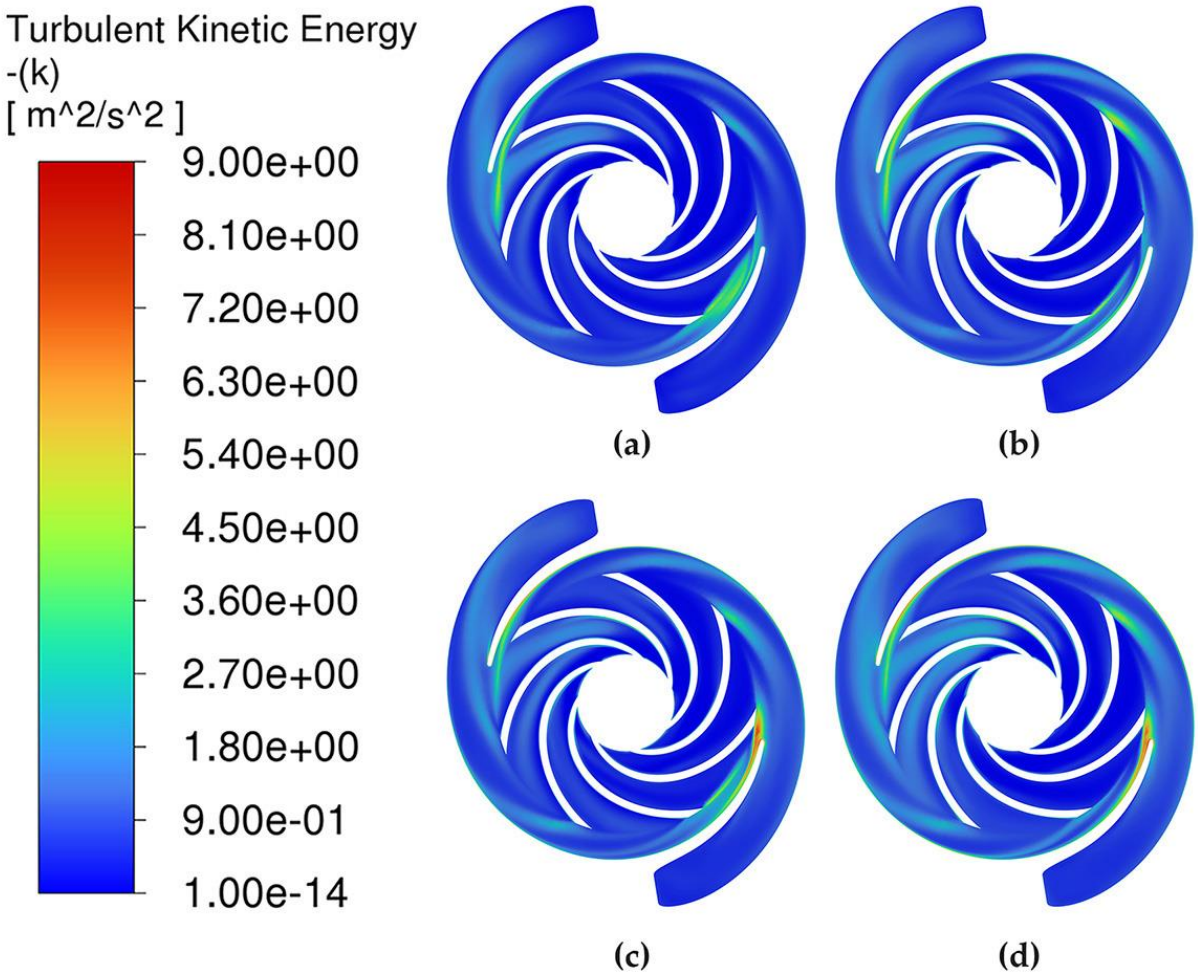

Figure 7. Turbulent kinetic energy k contours for 90 m³/h at the impeller outlet and volute tongue for varying surface roughness; from left to right (a) k_s = 0 μm (b) k_s = 25 μm (c) k_s = 50 μm (d) k_s = 73 μm

3.2. Experimental – CFD Results

It was observed that the numerical analysis with a wall roughness of k_s = 73 μm yields the closest agreement with the experimental results, and the comparison was therefore carried out based on this case. Figure 8 presents the comparison between the experimental and numerical data, while Table 3 summarises the differences in head and efficiency across all flow rates.

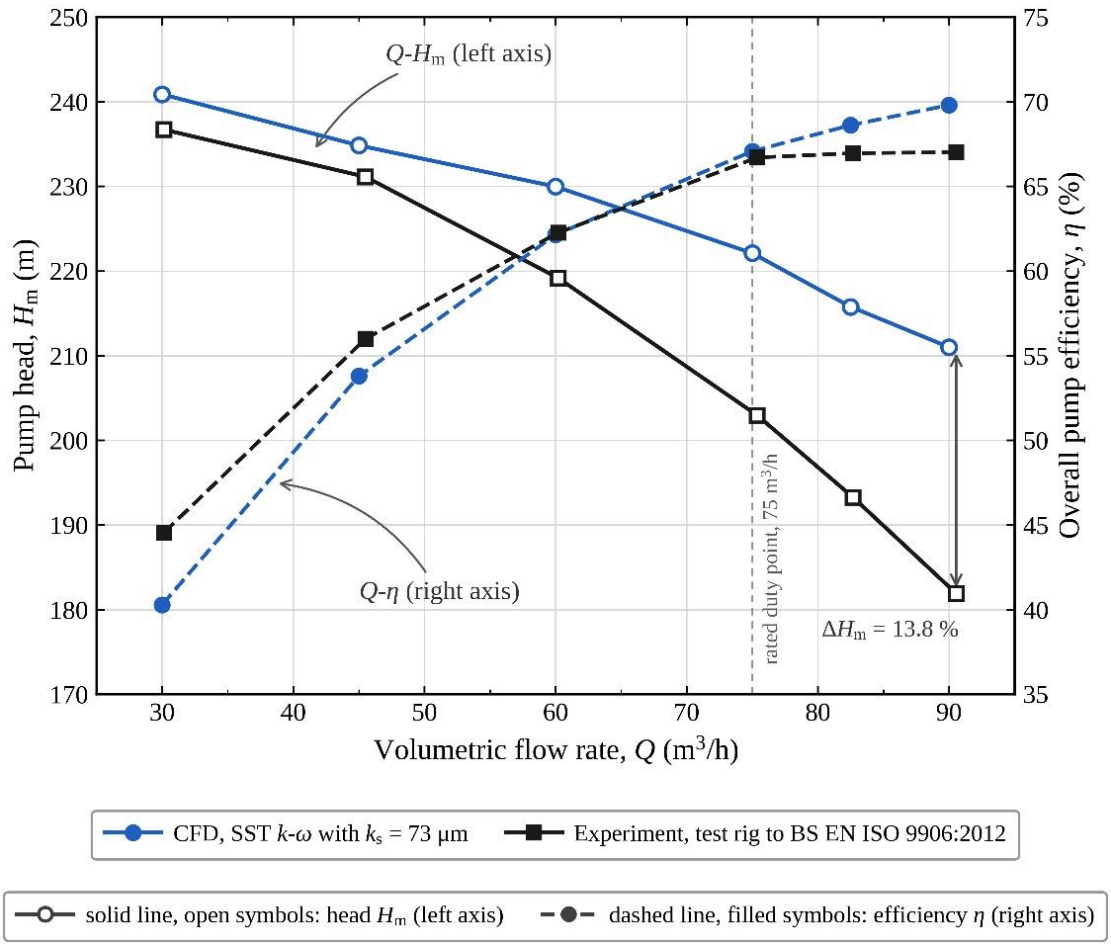

Figure 8. Experimental - CFD comparison

In terms of head, the experimental and numerical results exhibit a similar trend at low flow rates; however, the difference in head is observed to increase as the flow rate rises. While the deviation is 1.73% at 30 m³/h, it increases to 13.79% at 90 m³/h. Nevertheless, the overall shape and slope of the Q-H curves are broadly consistent between the numerical and experimental results.

Table 3. Comparison of CFD (k_s = 73 μm) and experimental results.

Q (m³/h)	Head H_m (m)			Overall efficiency η (%)		
	CFD	Experiment	ΔH_m (%)	CFD	Experiment	$\Delta\eta$ (%)
30	240.87	236.70	1.73	40.28	44.55	−10.59
45	234.83	231.12	1.58	53.79	55.99	−4.08
60	229.97	219.17	4.70	62.14	62.26	−0.20
75	222.10	202.94	8.63	67.07	66.70	0.54
82.5	215.77	193.26	10.43	68.61	66.96	2.41
90	211.00	181.90	13.79	69.80	67.01	3.99

In terms of efficiency, the sign of the deviation varies with flow rate. At 30 and 45 m³/h, the CFD efficiency is lower than the experimental one (≈−10.6% / ≈−4.1%), in the 60–75 m³/h range they are in close agreement, whereas at 82.5–90 m³/h the CFD efficiency is higher (≈+2.4% / ≈+4%). Although a head

difference of 13.79 % would be expected to be reflected to a similar extent in the efficiency deviation, the difference in efficiency remains at the level of only about 4% even at high flow rates.

The primary reason for this trend is that shrinkage-induced casting defects in the pump casing generate additional hydraulic losses in the experiment. The location and visual evidence of these local losses are detailed in the "Local Losses" section.

3.3. Local Losses

Due to casting difficulty and shrinkage in the pump casing, certain geometric imperfections formed after machining. The geometric defects shown in Figure 9 (protrusion–recess regions, sharp edges, and dimensional deviations) increase energy losses in the flow passage by inducing local velocity variations and turbulent regions. Since an ideal casing is used in the numerical model, these additional losses are not represented. The divergence between the experimental and CFD curves with increasing flow rate is consistent with the fact that such losses increase in proportion to the square of the velocity. The observed geometric imperfections are therefore regarded as the main cause of the reduction in head, as they enhance both frictional and form-related local loss components. The flow-rate dependence of this relationship is quantitatively confirmed by the growing difference between the experimental and CFD Q-H curves in the comparison.

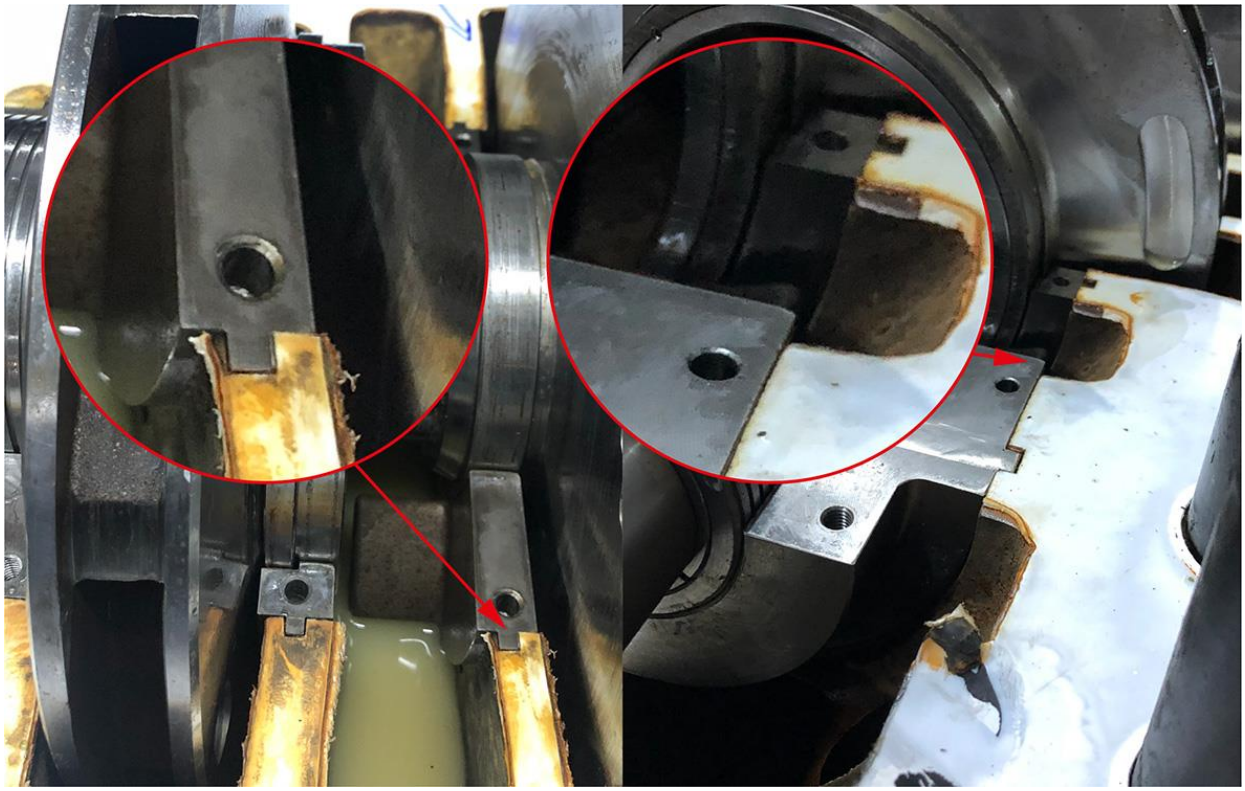

Figure 9. Geometric defects in the pump casing

3.4. Distribution of Moment Components

The total torque is decomposed into pressure and viscous components and presented in Table 4.

Table 4. Decomposition of the torque acting on the rotating walls into pressure and viscous components, at $Q = 90$ m³/h.

Stage	Component	Pressure moment (N·m)	Viscous moment (N·m)	Total moment (N·m)
Stage 1	Hub	−0.049	1.180	1.131
	Shroud	0.027	1.100	1.127
	Blade	55.393	1.533	56.925
	Tip	0.465	0.838	1.302
Stage 2	Hub	−0.034	1.144	1.110
	Shroud	0.020	1.158	1.178
	Blade	51.824	1.589	53.413
	Tip	−0.088	0.850	0.762
Stage 3	Hub	−0.015	1.308	1.293
	Shroud	0.019	1.123	1.142
	Blade	58.571	1.701	60.272
	Tip	0.032	0.832	0.864
Stage 4	Hub	−0.012	1.274	1.262
	Shroud	0.012	1.246	1.258
	Blade	51.067	1.763	52.830
	Tip	0.067	0.758	0.825
All stages		**217.30**	**19.40**	**236.70**

The static pressure forces exerted by the fluid on the blade surfaces generate the pressure moment and constitute the main component (approximately 97%) of the total torque on the blades. The static pressure contour shown in Figure 10 illustrates how the pressure field varies along the blade and indicates the regions where the pressure moment is dominant.

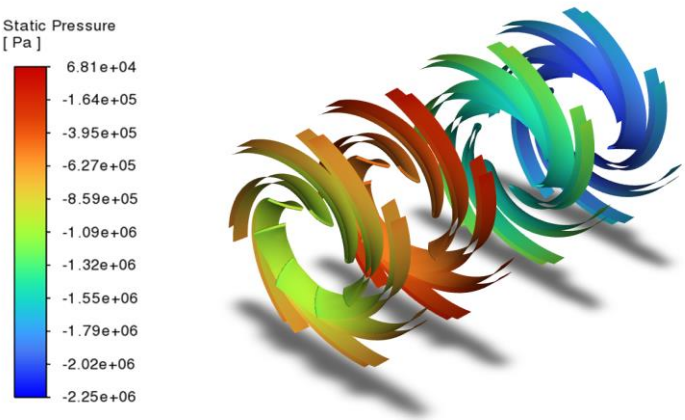

Figure 10. Static pressure distribution of blades

In the hub and shroud regions, almost all of the torque consists of the viscous component arising from wall friction. The shear stresses generated on the impeller surfaces due to the viscous effects of the fluid give rise to the viscous moment. The wall shear stress contour shown in Figure 11 highlights the areas where the viscous moment is effective and the regions where the interaction between the flow and the solid surfaces is most intense.

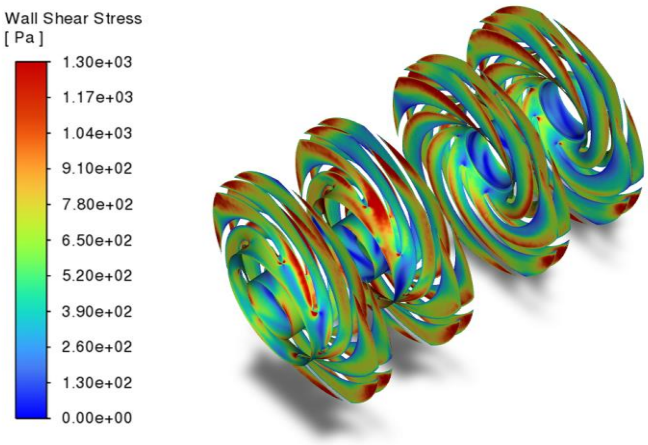

Figure 11. Wall shear stress on the hub and shroud surfaces

In the experimental pump, protrusions and geometric irregularities in the flow passage are expected to disturb the flow stability and to generate local vortex structures, particularly in the vicinity of the hub and shroud regions. These vortices increase the local velocity gradients, thereby enhancing viscous effects and, consequently, the viscous moment. The reduction in head leads to a decrease in the static pressure field on the blade surfaces and thus to a reduction in the pressure moment.

As a result of the combined influence of these two effects, the pressure moment generated by the blades decreases (reflecting the drop in hydraulic head), while the viscous moment in the hub–shroud regions increases and is thought to partially compensate the total torque. In other words, although the hydraulic power loss increases, the total torque is expected to exhibit only a more limited reduction due to the rise in viscous moment. This behaviour explains why the difference in head between CFD and experiment is not reflected to the same extent in the efficiency reduction.

4. CONCLUSIONS

In this study, the experimental and numerical results for a BB3-type pump at different surface roughness levels (k_s = 0, 25, 50, and 73 μm) were compared, and the influence of surface roughness on the Q–H_m and Q–η characteristics was evaluated in an integrated manner. The validation analyses showed that the numerical model captures the pump characteristic with sufficient accuracy. In particular, the solution with ks = 73 μm provides the best quantitative agreement with the experimental curves and keeps the deviation in overall efficiency within about 4.1% in the 45–90 m³/h range; however, at the lowest flow rate (30 m³/h) a larger discrepancy is observed due to deep part-load operation. While at high flow rates the experiment–CFD discrepancy in head (Hm) reaches up to 13.79%, this discrepancy is markedly lower at low flow rates. The increase in deviation with flow rate is consistent with the increase in local losses proportional to the square of the velocity.

Increasing roughness systematically reduces both head and efficiency along the characteristic; near the best-efficiency region, increasing ks from 0 to 73 μm leads to head penalties of up to 5.94% and relative

efficiency losses of 6.62%, respectively. These trends are associated with higher wall shear stress and enlarged high-turbulence regions, especially at the impeller outlet and volute tongue.

From a manufacturing-tolerance standpoint, the results indicate that realistic as-cast surface conditions and casing irregularities are the main contributors to these performance penalties, highlighting that surface-finish requirements and casting tolerances for high-pressure BB3 pumps should be specified with their hydraulic impact in mind. From a CFD-modelling standpoint, the study shows that assuming hydraulically smooth walls can lead to noticeable overprediction of head at high flow rates, whereas incorporating realistic sand-grain roughness and ensuring adequate near-wall resolution limits the efficiency discrepancy to about 4% and enables reliable prediction of the Q–H and Q–η curves.

Declaration of Ethical Standards

The authors declare that all ethical standards have been followed in the preparation of this manuscript. The experiments reported in this study were performed on an industrial pump test rig and did not involve human participants or animals; therefore, formal ethics committee approval was not required.

Credit Authorship Contribution Statement

Sinan Güngör: Writing – original draft, Methodology, Investigation (experimental pump testing), Formal analysis, Data curation, Software (CFD modelling and numerical simulations), Validation, Visualization. **Abdulkerim Okbaz:** Writing – review & editing, Supervision, Methodology, Conceptualization. **Zehra Yumurtacı:** Writing – review & editing, Conceptualization, Supervision, Project administration.

Declaration of Competing Interest

No potential conflicts of interest were reported by the authors in relation to this study.

Funding / Acknowledgements

No external financial support or research grant was received for this study. The experimental tests were carried out at the test laboratory of Standart Pompa. The authors gratefully acknowledge Standart Pompa for providing the experimental facilities and technical support that contributed to the completion of this research.

Data Availability

Research data related to this article can be obtained from the corresponding author upon a justified request.

Use of Artificial Intelligence

OpenAI ChatGPT was used solely to improve the English language quality, grammar, and readability of the manuscript during its preparation and revision. The AI tool was not used to generate scientific content, research data, interpretations, analyses, or results. All AI-assisted revisions were reviewed and verified by the authors, who remain fully responsible for the accuracy, originality, and integrity of the manuscript.

5. REFERENCES

[1] A. J. Stepanoff, *Centrifugal and Axial Flow Pumps: Theory, Design and Application*. Krieger Pub. Co., 1993.

[2] S. Lazarkiewicz and A. Troskolanski, *Impeller Pumps*, 1st ed. Warsaw: Pergamon Press, 1965.

[3] American Petroleum Institute, *Centrifugal Pumps for Petroleum, Petrochemical, and Natural Gas Industries*, 12th ed. Washington DC: American Petroleum Institute, 2021.

[4] Z. Mohammadian, H. Ayremlouzadeh, and A. Doniavi, "Numerical investigation on the effect of mold design on shrinkage of sand casted multistage BB3-6x6 pump casing," *International Journal of Engineering, Transactions B: Applications*, vol. 29, no. 8, pp. 1175–1182, Aug. 2016, doi: 10.5829/idosi.ije.2016.29.08b.18.

[5] C. Wang *et al.*, "Optimal design of multistage centrifugal pump based on the combined energy loss model and computational fluid dynamics," *Appl. Energy*, vol. 187, pp. 10–26, Feb. 2017, doi: 10.1016/j.apenergy.2016.11.046.

[6] R. N. Pinto, A. Afzal, L. V. D'Souza, Z. Ansari, and A. D. Mohammed Samee, "Computational Fluid Dynamics in Turbomachinery: A Review of State of the Art," *Archives of Computational Methods in Engineering*, vol. 24, no. 3, pp. 467–479, Jul. 2017, doi: 10.1007/s11831-016-9175-2.

[7] K. Ulaganathan and P. Karuppuswamy, "Study the effects of surface coating on impeller and volute casing to improve the efficiency of the water pump," *Desalination Water Treat.*, vol. 132, pp. 79–88, Nov. 2018, doi: 10.5004/dwt.2018.23055.

[8] O. Kocaaslan, M. Ozgoren, M. H. Aksoy, and O. Babayigit, "Experimental and numerical investigation of coating effect on pump impeller and volute," *Journal of Applied Fluid Mechanics*, vol. 9, no. 5, pp. 2475–2487, 2016, doi: 10.18869/acadpub.jafm.68.236.25094.

[9] P. A. Deshmukh, K. D. Deshmukh, and N. A. Mandhare, "Performance enhancement of centrifugal pump by minimizing casing losses using coating," *SN Appl. Sci.*, vol. 2, no. 2, Feb. 2020, doi: 10.1007/s42452-020-2042-7.

[10] V. Papageorgiou, G. Mansour, and I. Chouridis, "Improving Centrifugal Pump Performance and Efficiency Using Composite Materials Through Additive Manufacturing," *Machines*, vol. 13, no. 8, Aug. 2025, doi: 10.3390/machines13080729.

[11] A. Lipej, S. Muhic, and D. Mitruševski, "Wall roughness influence on the efficiency characteristics of centrifugal pump," *Strojniski Vestnik/Journal of Mechanical Engineering*, vol. 63, no. 9, pp. 529–536, 2017, doi: 10.5545/sv-jme.2017.4526.

[12] X. He *et al.*, "Influence of critical wall roughness on the performance of double-channel sewage pump," *Energies (Basel).*, vol. 13, no. 2, 2020, doi: 10.3390/en13020464.

[13] S. E. Lim and C. H. Sohn, "CFD analysis of performance change in accordance with inner surface roughness of a double-entry centrifugal pump," *Journal of Mechanical Science and Technology*, vol. 32, no. 2, pp. 697–702, Feb. 2018, doi: 10.1007/s12206-018-0117-1.

[14] B. Liang, M. Wang, Q. Zhang, Z. Wang, and P. Jiang, "Influence of wall roughness on pressure distribution and performance of centrifugal dredge pumps," *Intelligent Marine Technology and Systems*, vol. 1, no. 1, Dec. 2023, doi: 10.1007/s44295-023-00004-1.

[15] H. Chang, Z. Wang, G. Peng, W. Shi, R. Lin, and L. Zhou, "Role of wall roughness on energy dissipation and vortex dynamics in self-priming centrifugal pump: A study via entropy generation and Liutex vortex identification," *Energy*, vol. 337, Nov. 2025, doi: 10.1016/j.energy.2025.138733.

[16] B. Torner, D. V. Duong, and F. H. Wurm, "Numerical Determination of the Equivalent Sand Roughness of a Turbopump's Surface and Its Roughness Influence on the Pump Characteristics," *International Journal of Turbomachinery, Propulsion and Power*, vol. 8, no. 1, Mar. 2023, doi: 10.3390/ijtpp8010005.

[17] H. Benigni, H. Jaberg, H. Yeung, T. Salisbury, O. Berry, and T. Collins, "Numerical simulation of low specific speed American petroleum institute pumps in part-load operation and comparison with test rig results," *Journal of Fluids Engineering, Transactions of the ASME*, vol. 134, no. 2, 2012, doi: 10.1115/1.4005769.

[18] K. Juckelandt, S. Bleeck, and F.-H. Wurm, "Analysis of losses in centrifugal pumps with low specific speed with smooth and rough walls," in Proc. European Conference on Turbomachinery Fluid dynamics & Thermodynamics, Madrid, Spain, Mar. 2015. [Online]. Available: www.euroturbo.eu

[19] *BS EN ISO 9906:2012 Rotodynamic pumps - Hydraulic performance acceptance tests - Grades 1, 2 and 3*. London: BSI Standards Limited, 2012.

[20] J. F. Gülich, *Centrifugal Pumps*, 4th ed. Villeneuve, Switzerland: Springer, 2020.

[21] M. N. Kaya, "Shock-Boundary Layer Interaction in Transonic Flows: Evaluation of Grid Resolution and Turbulence Modeling Effects on Numerical Predictions," *CMES - Computer Modeling in Engineering and Sciences*, vol. 145, no. 1, pp. 327–343, 2025, doi: 10.32604/cmes.2025.072000.

[22] I. E. Idel'chik, *Handbook of Hydraulic Resistance*. Hemisphere Pub. Corp., 1986.